

Supporting information for Interplay of seismic and a-seismic deformation during the 2020 sequence of Atacama, Chile.

E. Klein^{1,*}, B. Potin², F. Pasten-Araya², R. Tissandier³, K. Azua², Z.

Duputel⁴, C. Herrera⁵, L. Rivera⁴, J.M. Nocquet^{3,6}, J.C. Baez⁷, D. Zigone⁴,

R. Madariaga^{1,2}, J.P. Ampuero⁶, S. Ruiz², C. Vigny¹

¹Laboratoire de géologie - CNRS UMR 8538, Ecole normale supérieure - PSL University, Paris, France

²Departamento de Geofísica, Universidad de Chile, Santiago, Chile

³Université de Paris, Institut de Physique du Globe de Paris, CNRS, F-75005 Paris, France

⁴Institut Terre et Environnement de Strasbourg, Université de Strasbourg/EOST/ENGEES, CNRS UMR 7063, 5 rue Descartes, Strasbourg F-67084, France

⁵School of Earth and Ocean Sciences, University of Victoria, 3800 Finnerty Road, Victoria, British Columbia V8P 5C2, Canada

⁶Université Côte d'Azur, IRD, CNRS, Observatoire de la Côte d'Azur, Géoazur, 250 rue Albert Einstein, Sophia Antipolis, 06560 Valbonne, France

⁷Centro Sismológico Nacional Universidad de Chile Blanco Encalada 2002 Santiago CP 8370449, Chile

E., Klein: klein@geologie.ens.fr

Contents of Supporting information

1. Figures S1 to S12

2. Table S1 to S3

3. Two animations showing the aftershock spatio-temporal evolution over the first 72 hours and the postseismic slip evolution are also provided as separate supplementary materials.

Seismic Analysis.: Table S1 gathers the focal mechanism parameters re-estimated for the largest 3 events (section 2.2). Fig. S1 gathers the results of the characterisation of the sequence: Mainshock-Aftershock sequence or Seismic swarm.

GPS data analysis: Figure S2 shows how the CGPS daily process was made on the day of the earthquake, excluding observations during the periods represented by the gray areas. Table S2 gathers the coseismic offsets estimated from daily CGPS for the mainshock and the largest aftershock. It appeared impossible to extract any coseismic offset for the aftershock of 4:30 UTC.

Figures S3 and S4 illustrate the sidereal filtering that is applied on HRGPS data, with the example of the station HSCO. Figs. S5 to S7 show the filtered motograms for the 3 largest earthquakes of the sequences and table S3 gathers the coseismic offsets estimated from HRGPS for the mainshock and the largest aftershock. Fig. S7 shows that no static displacements is detectable for the aftershock of 4:30 UTC.

Note that most of the displacements are small, ranging between 1 and 15 mm. Models inferred from these displacements rest on the trust we place in GPS ability to quantify

small displacements of several millimeters only. In our case, all GPS stations are at more than 10 km and less than 1000 km from the earthquake and from each other. These are neither short nor long distances and in this range the precision of GPS is rather flat, around 1-2 mm for the horizontal components. The precision of station displacements rather varies because some stations have better data than others (better sky coverage, less obstacles, better electronics...). The fact that different stations have different uncertainties is quantified during the GPS data processing (see section 3.2) and taken into account in the modelling. Displacements sticking out of their uncertainty ellipse are considered significant, regardless of their amplitude or their distance to the epicenter.

Evaluating the spatial resolution: In order to evaluate the spatial resolution provided by our network of cGPS stations, we performed three types of tests. First, we performed a checkerboard test (Fig. S11), building an input model with patches of $\sim 40 \times 40$ km, calibrated on the size of the aftershock. Unsurprisingly, we do not have resolution over the first 15 km or so of the slab, which is a very standard results for GNSS measurements in Chile, considering the distance between the trench and the coast (of the order of 100 km). We also loose resolution deeper than 50km and towards South where we miss several stations. But we recover the pattern quite well between depths of 15 and 50 km and between 27°S and 28.5°S , which includes the region of the 2020 sequence. This is still the case when we add a ± 2 mm white noise to the data: resolution decreases a bit, but recovery of the patches in the area of the 2020 sequence remains good. However, a checkerboard of a given size is a more difficult pattern to invert than a single event of the same size. In the case of a single event, even small, GPS vectors would converge towards the source, which they don't do with the checkerboard because it is pulling them towards all directions. It is only the gradients between vectors (small numbers) that allow to re-

trieve the checkerboard when the actual vectors (larger numbers) allow to retrieve a single source. Therefore, we next performed localization tests (Fig. S12) in which we invert for sources of the size of the aftershock, changing of localization within the region where the swarm occurred. In all cases, the inversion recovers correctly the synthetic input event location and slip-distribution, especially if located between 20-30 km depth. Inverted slip distributions are slightly wider (10%) and with lower peak slip (by 10-30%), which illustrates a) the (slight) smearing due to smoothing parameters and b) the trade-off between the size of the slip area and the amount of slip distributed over this area. Recovered magnitudes are generally larger by 0.1 than the input magnitudes, which explains well the slightly larger geodetic magnitude we inferred compared to the seismologic one (6.5 vs. 6.4, see section 4.1 on the main paper). Finally, we performed smearing tests (Fig. S13) inverting for a synthetic input model that looks like the aftershock distribution, but without slip 25 mm (ie, a more concentrated slip distribution). Both inversions (with perfect or artificially degraded GPS data), recover a more spread distribution, adding small slip mostly updip the rupture zone. That is because of a) smearing related to smoothing parameters in the inversion and b) the previously demonstrated lesser resolution towards smaller depth. However, we do not see much smearing (added slip) downdip the rupture (under the coastline) nor along-strike the subduction (north or south), which is an indication that the data constrain well the slip distribution. As we artificially increase the noise of the GPS data, slip starts to be inverted here and there, where lesser resolution allows it to appear: i.e. at depth. Consistently, the recovered magnitude increases: 6.58 (C) wrt 6.38 (B) and 6.29 (A). Constraining the magnitude to a known value (applicable in the case of an earthquake, not for a slow-slip) would prevent this to happens.

Coseismic slip static inversions: Starting from the preferred slip distribution, we explore the trade-off between the peak slip and the size of the rupture zone. To do so, we first forbid slip smaller than 60 mm which reduce the size of the rupture zone. In order to match the M_w of the preferred distribution, we double the slip amplitude (Fig. S8-B). We find a reasonable fit to data, particularly to the south of the rupture zone, highlighting the limited resolution there. However, we observe a significantly larger residual at BAR2, which is one of the stations with the largest coseismic offset. Going further, we repeat the method, forbidding slip smaller than 80 mm, to reach a rupture zone of about $30 \times 30 \text{ km}^2$, with the slip amount multiplied by 4 to match the M_w . We now observe a significantly worse fit to data at all the closest stations (BAR2, TTRL and LLCH). Therefore, the orientation of most stations, that are not converging toward a pin point, justifies the extension of the slip distribution.

We tested a model with a pure dip slip direction, perpendicular to the trench (see Fig. S9-B). The rupture zone is slightly shifted northward compared to preferred model (Fig. S9-A), to reproduce the displacements measured further away in the Northeast (UDAT, TAMR), together with more deep slip. However, this distribution could not reproduce the displacement direction of both near-field stations (BAR2 and TTRL), neither the atypical southward motion observed at stations located south of the event (LLCH, HSCO). Finally, we tested a model allowing two directions of slip. This model unsurprisingly provides the smallest residuals on the data (because the number of fault parameters is doubled), but shows chaotic slip directions and larger deep slip (Fig. S9-C) which does not seem mandatory to fit the data (see Fig. S9-A). Therefore, we do not consider this model any further. We also show in Fig. S10 the preferred models for both the main shock and the aftershock, with slip values of the fault patches represented as punctual

circles, to illustrate the fault spatial resolution of the fault geometry.

Dynamic inversions: Figure S14 shows the main shock waveforms, observed and modeled from the best model presented in the main paper on section 4.3.

Interplay between seismic and aseismic slip: Figure S15 compares the results of the static and the cumulative kinematic slip distributions of postseismic displacements after 22 days (between September, 2nd and September 24th, which are produced following 2 different and independent methodologies. Slip distributions are shown on Fig. S15, represented with the same color scale. We find very similar slip distributions with the main slip region at the same location offshore and some deep slip located further north. The static model features more slip, and an additional patch in the south.

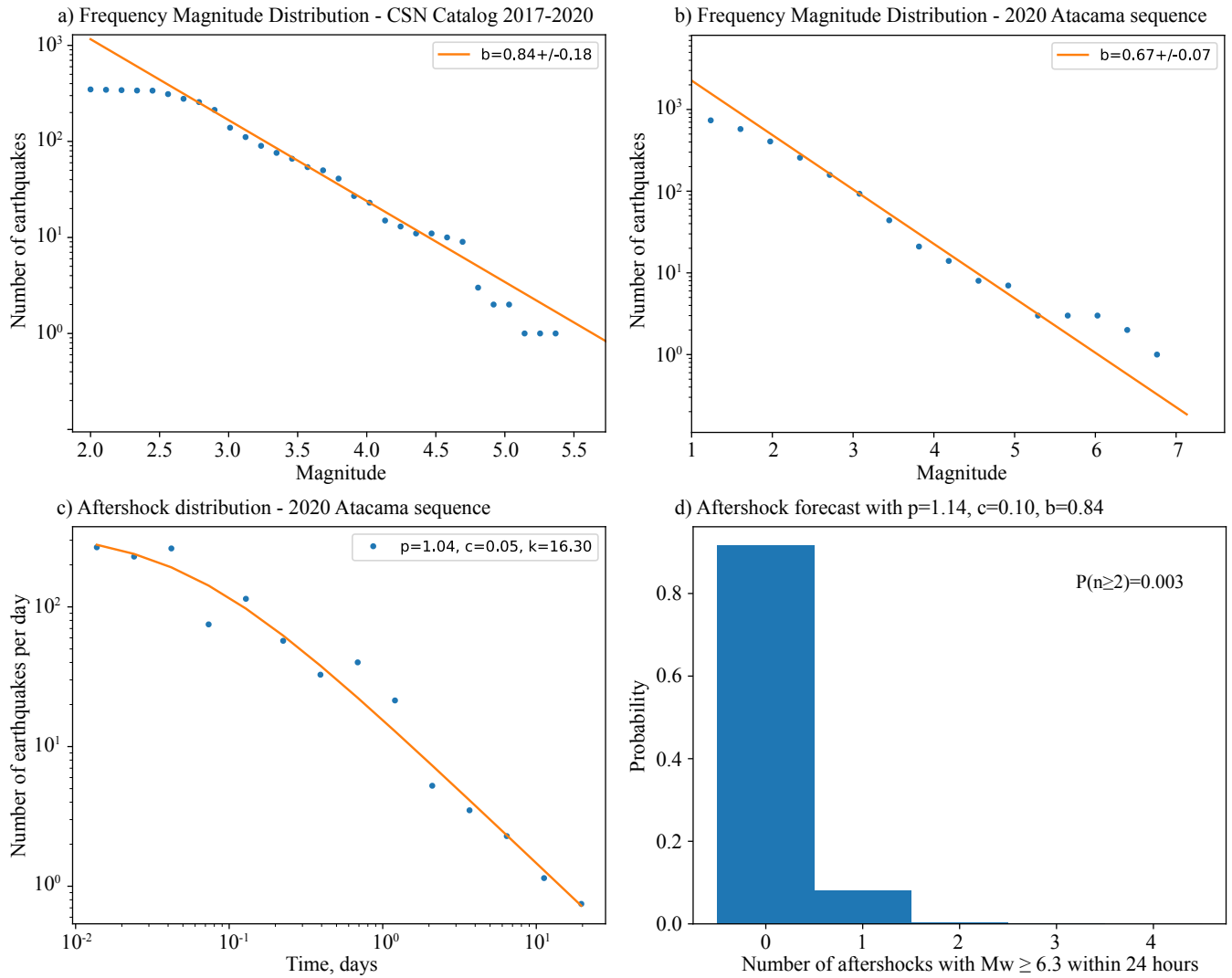


Figure S1. Magnitude and temporal distribution of earthquakes during the 2020 Atacama sequence. a) Frequency Magnitude Distribution of the CSN catalog since January 2017. b) Frequency Magnitude Distribution of the Atacama sequence (from 2020/09/01 until 2020/09/25). c) Aftershocks per day against time during the 2020 Atacama sequence. d) Forecast of aftershock activity within 24 hours after the mainshock.

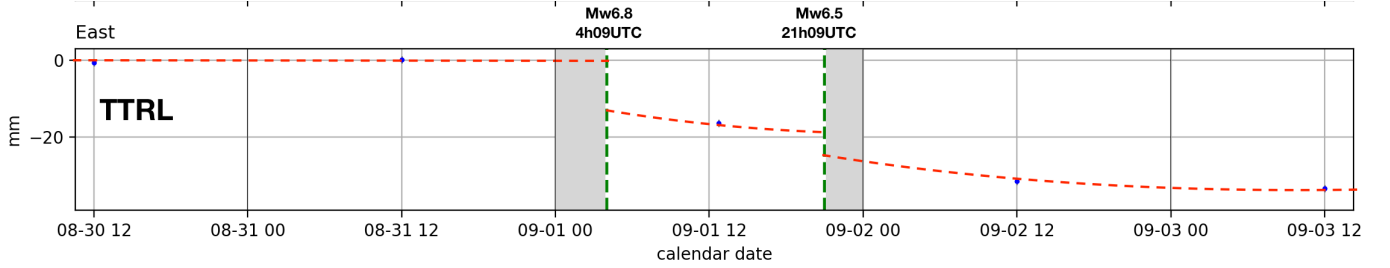


Figure S2. Processing of the position of day 245: TTRL East time series centered on the 1st of September with 2 days before and 2 days after. The gray areas illustrate the periods eliminated from the processing.

Event time	Typical focal mechanism				Bootstrap	
	hh:mm	strike	dip	rake	M_w	$\langle M_w \rangle \pm 2\sigma$
04:09	9.8°	16.8°	103.9°	6.90	5.87	± 0.07
04:30	25.6°	11.8°	125.1°	6.30	6.29	± 0.04
21:09	18.9°	18.8°	118.2°	6.40	6.42	± 0.07

Table S1. **W-phase focal mechanisms and M_w bootstrap.** For each of the three main events, the table presents a typical focal mechanism and moment magnitude as well as the bootstrap mean $\langle M_w \rangle$ with the corresponding $\pm 2\sigma$ uncertainty. (cf section 2.2).

HUASCO

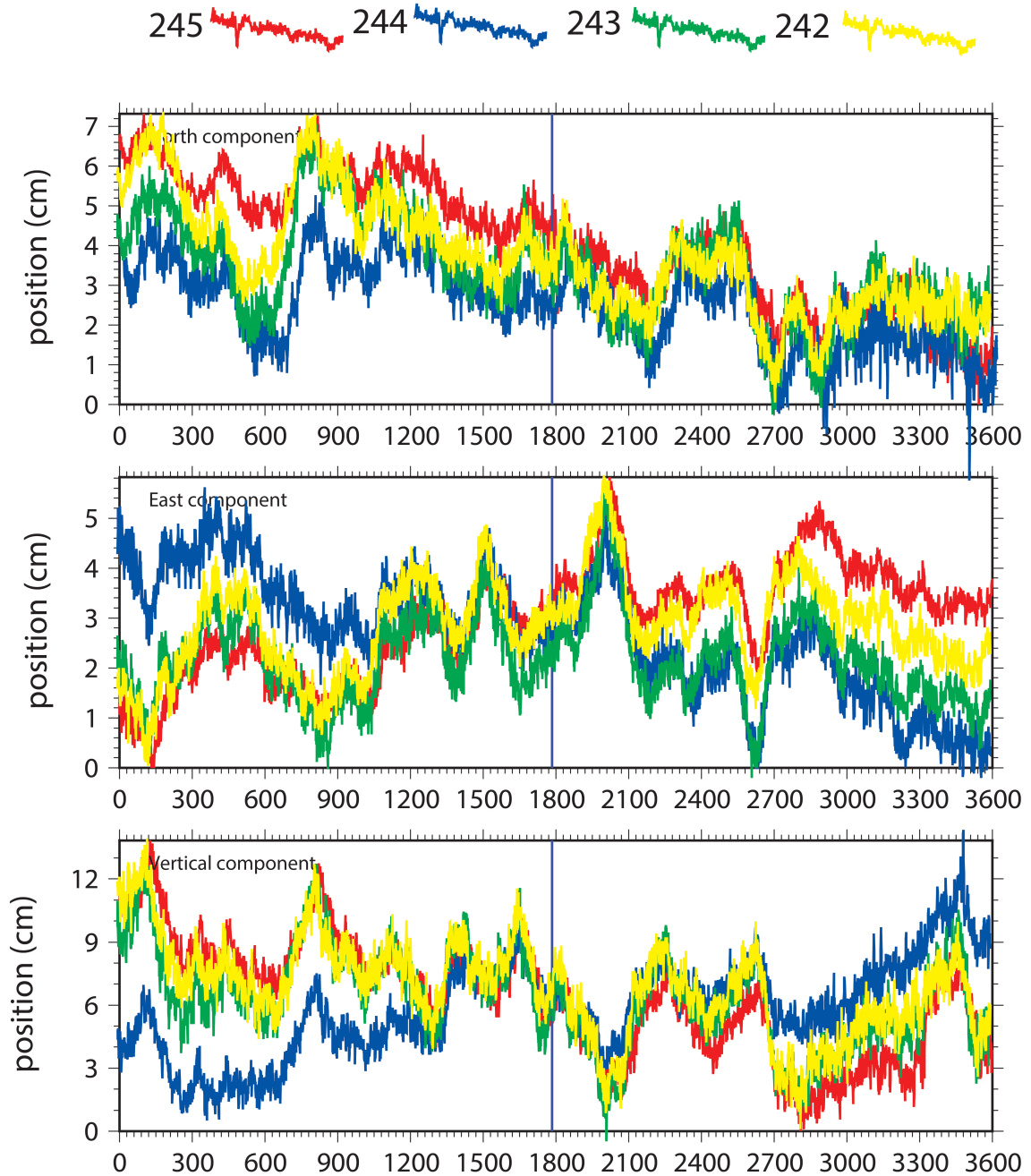


Figure S3. Motogramms at HSCO as function of time. We show 4 days (245, 244, 243 and 242) over 1 hour segment around the same time every day (4m7s shift every day). A clear common mode shows up on all 3 components.

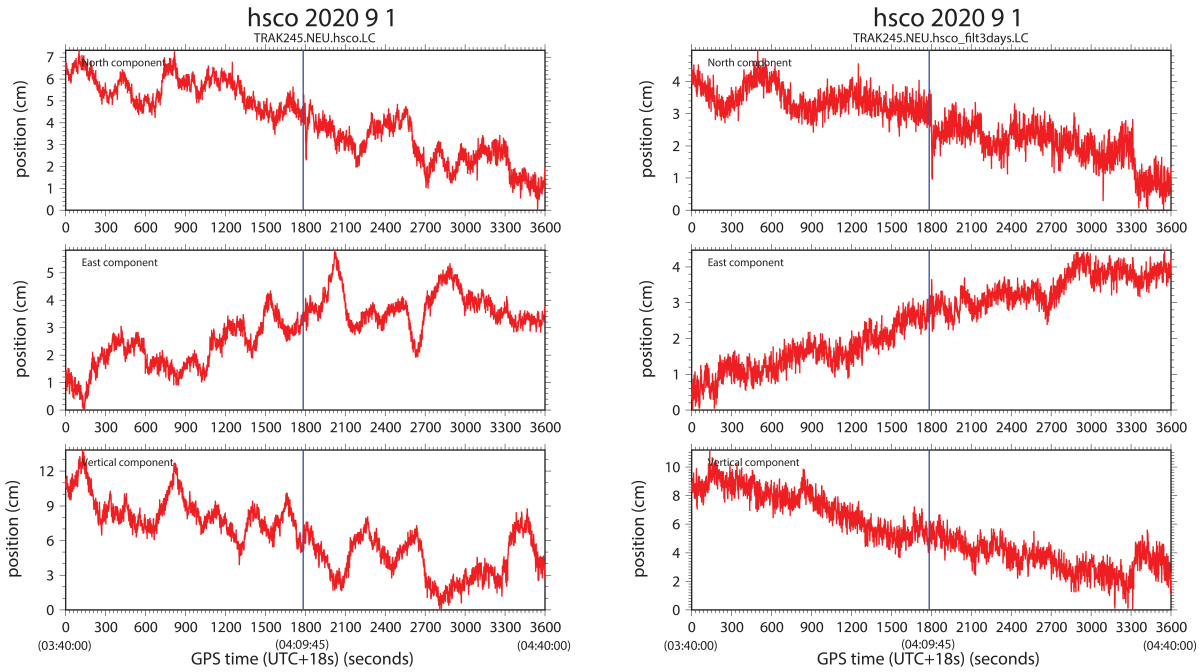


Figure S4. Motogramms at HSCO day 245, 1 hour segment around the earthquake. raw motogramm left, filtered motogramm using a 3 day-sideral filter right.

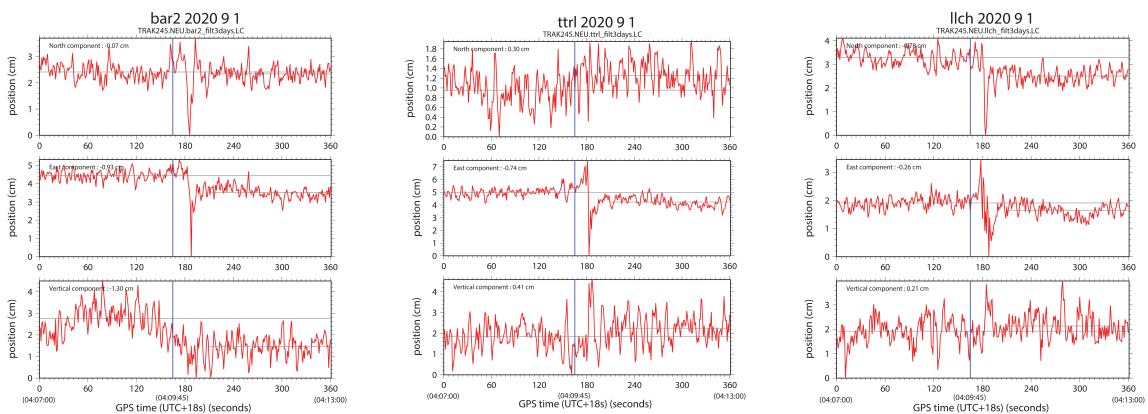


Figure S5. Filtered motogramms and co-seismic offset estimation at BAR2, TTRL and LLCH for the main shock of 4:09.

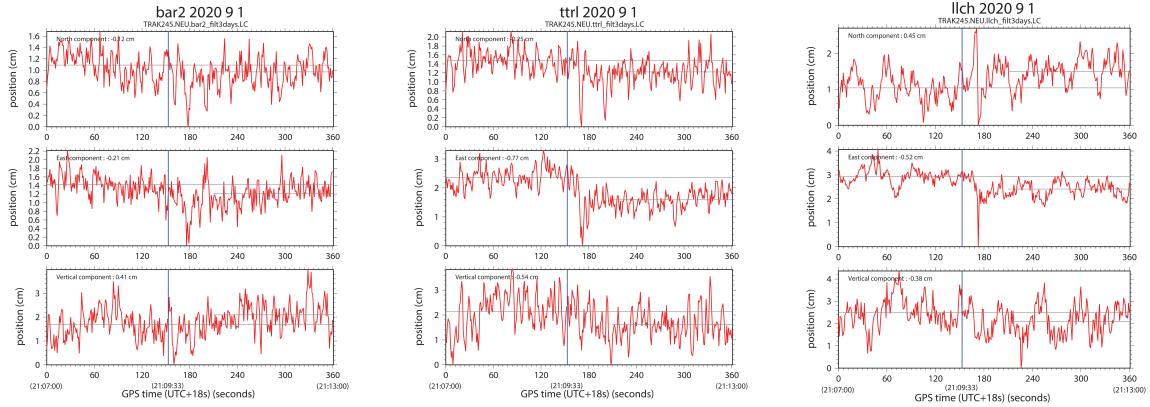


Figure S6. Filtered motogramms and co-seismic offset estimation at BAR2, TTRL and LLCH for the aftershock of 21:09.

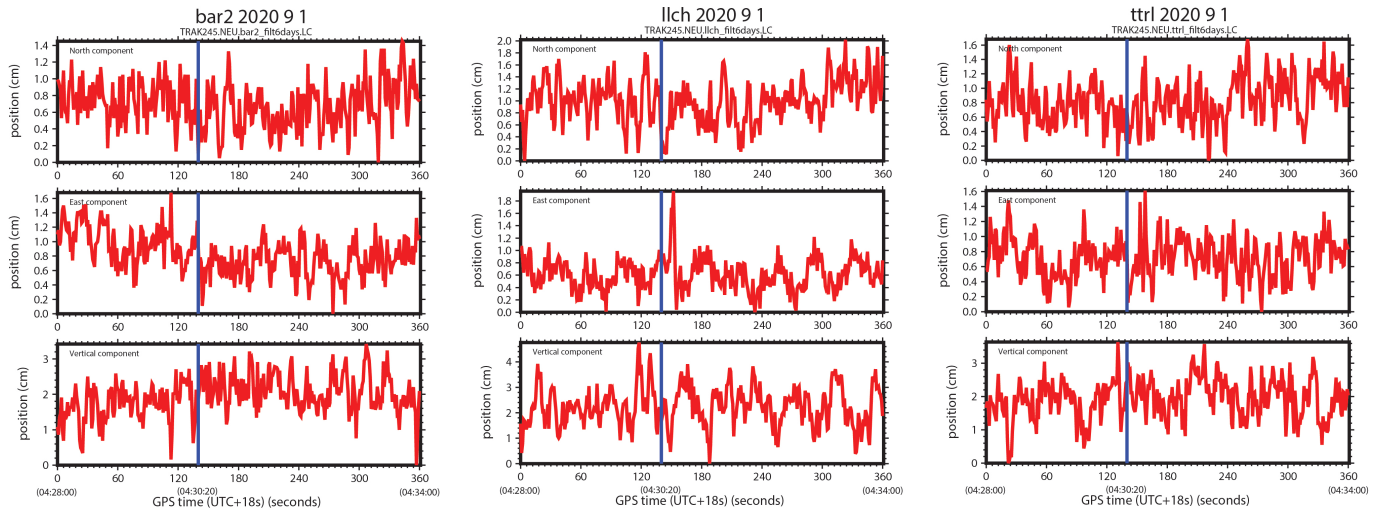


Figure S7. Filtered motogramms at nearest stations BAR2, LLCH and TTRL around the time of the smaller aftershock (M_w 6.3) of 04:h30 UTC. No static offset detectable

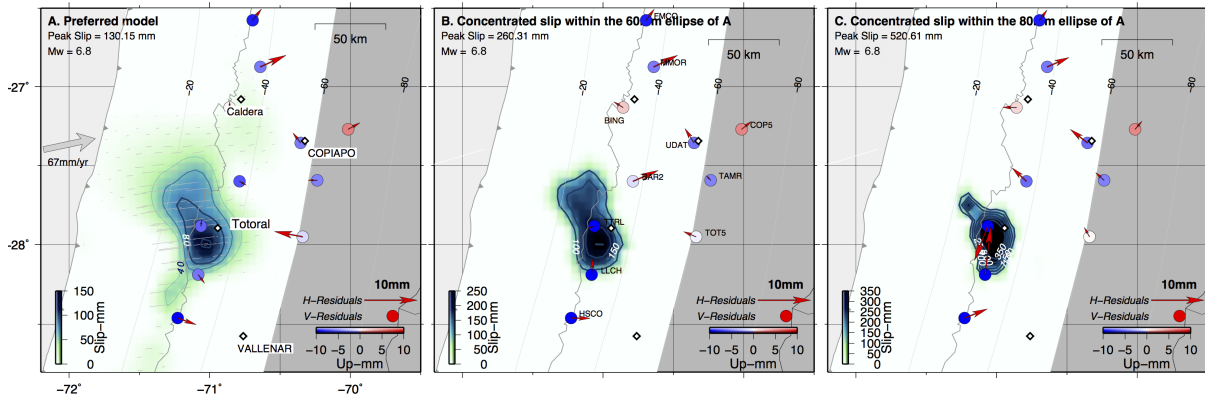


Figure S8. A) Preferred model presented on Fig.6-A; B) Slip distribution obtained doubling the slip amount within the 60 mm region of the preferred model and forbidding slip < 60 mm; C) Slip distribution obtained doubling the slip amount within the 80 mm region of the preferred model and forbidding slip < 80 mm. A different color scale is used for each model. In the 3 cases, we show the residuals, with vectors depicting the horizontal ones and the polar-colored dots the vertical ones.

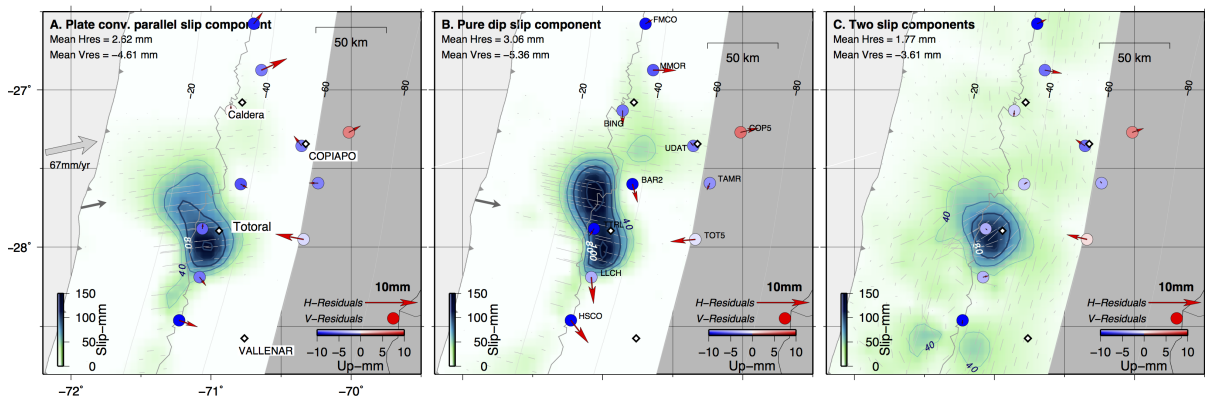


Figure S9. A) Preferred model presented on Fig.6-A; B) slip distribution obtained with a pure dip slip component (trench perpendicular); C) Slip distribution obtained with a two slip components model (trench parallel and trench perpendicular). The same color scale is used, the blue isolines are given every 20 mm. The dark gray arrow on the trench shows in A and B the unique slip direction used in the inversion. Slip directions on each patch are also represented by the light gray lines on top of the 3 slip distributions. In the 3 cases, we show the residuals, with vectors depicting the horizontal ones and the polar-colored dots the vertical ones.

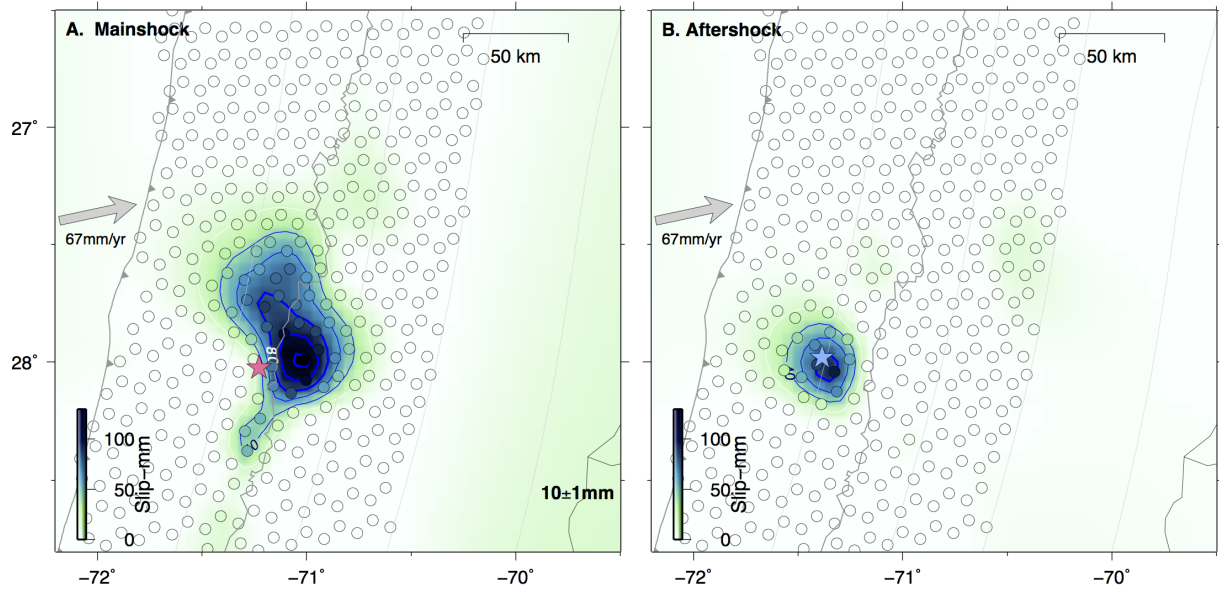


Figure S10. A) Preferred model of the mainshock, presented on Fig.6-A ; B) Preferred model of the aftershock of 21:00 UTC, presented on Fig. 6-B; The same color scale is used for both models and we show slip values on the fault patches to illustrate the fault spatial resolution.

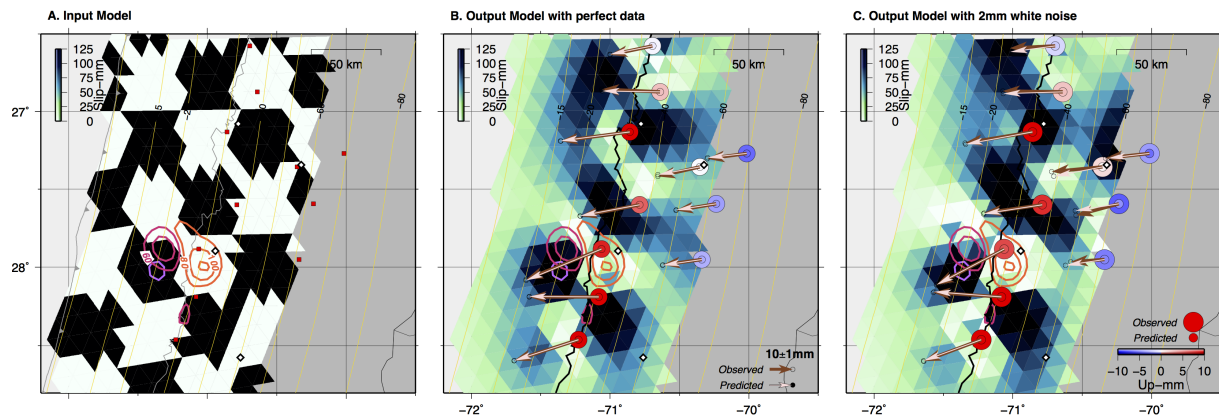


Figure S11. A) Input model with patches of $0.4^\circ \times 0.4^\circ$ corresponding to the size of the M_w 6.4 aftershock, the amplitude of slip is also calibrated based on the aftershock. Two inversions are performed, B) with ‘perfect data’ associated with uncertainties of 1 mm; C) with data deteriorated with white noise of 2 mm of std, associated with the same uncertainties. The slip triangles depict the discretization of the mesh describing the subduction trench. The slip distribution of the 3 events (M_w 6.8, early-afterslip, M_w 6.4) are represented with colored contours for the purpose of localization.

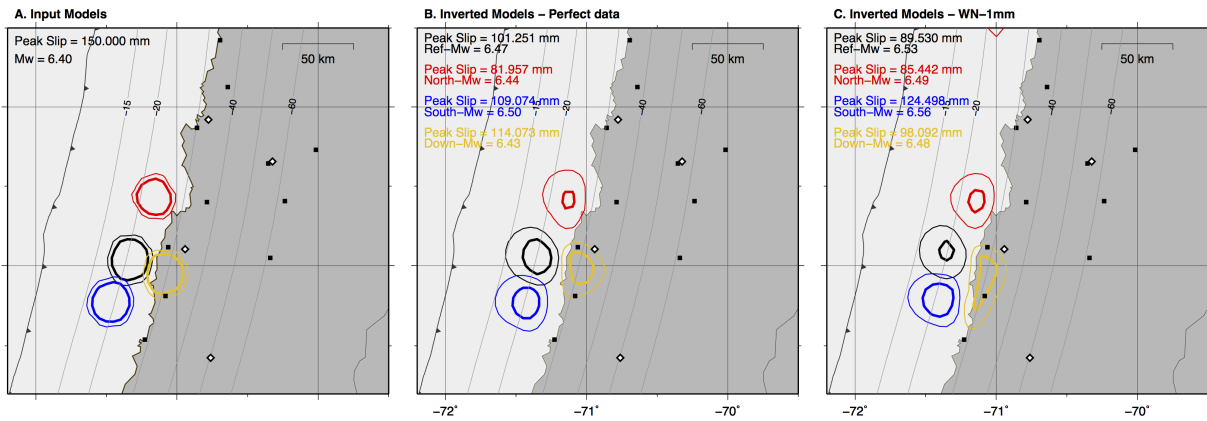


Figure S12. A) Input models with varying localization and identical slip distributions, calibrated to match the size and M_w 6.4 of the aftershock. The black model corresponds to the location of the aftershock. Two inversions are performed, B) with ‘perfect data’ associated with uncertainties of 1 mm; C) with data deteriorated with white noise of 1 mm of std with the same uncertainties. The vertical component is not used in the inversion, similarly to the aftershock inversion. Slip contours of 40 mm (thin contours) and 80 mm (thick contours) are depicted similarly to the real earthquakes slip distributions in the paper.

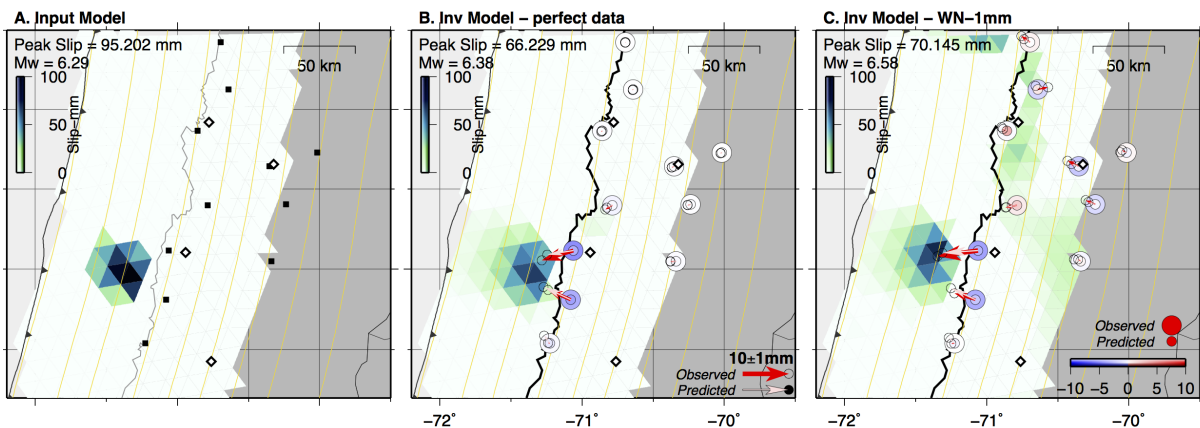


Figure S13. A) Input model (corresponding to the distribution of the afterslip but without slip smaller than 25 mm). B) inverted with ‘perfect data’ associated with uncertainties of 1 mm; C) inverted with data deteriorated with white noise of 1 mm of std with the same uncertainties. The vertical component is not used in the inversion, similarly to the aftershock inversion.

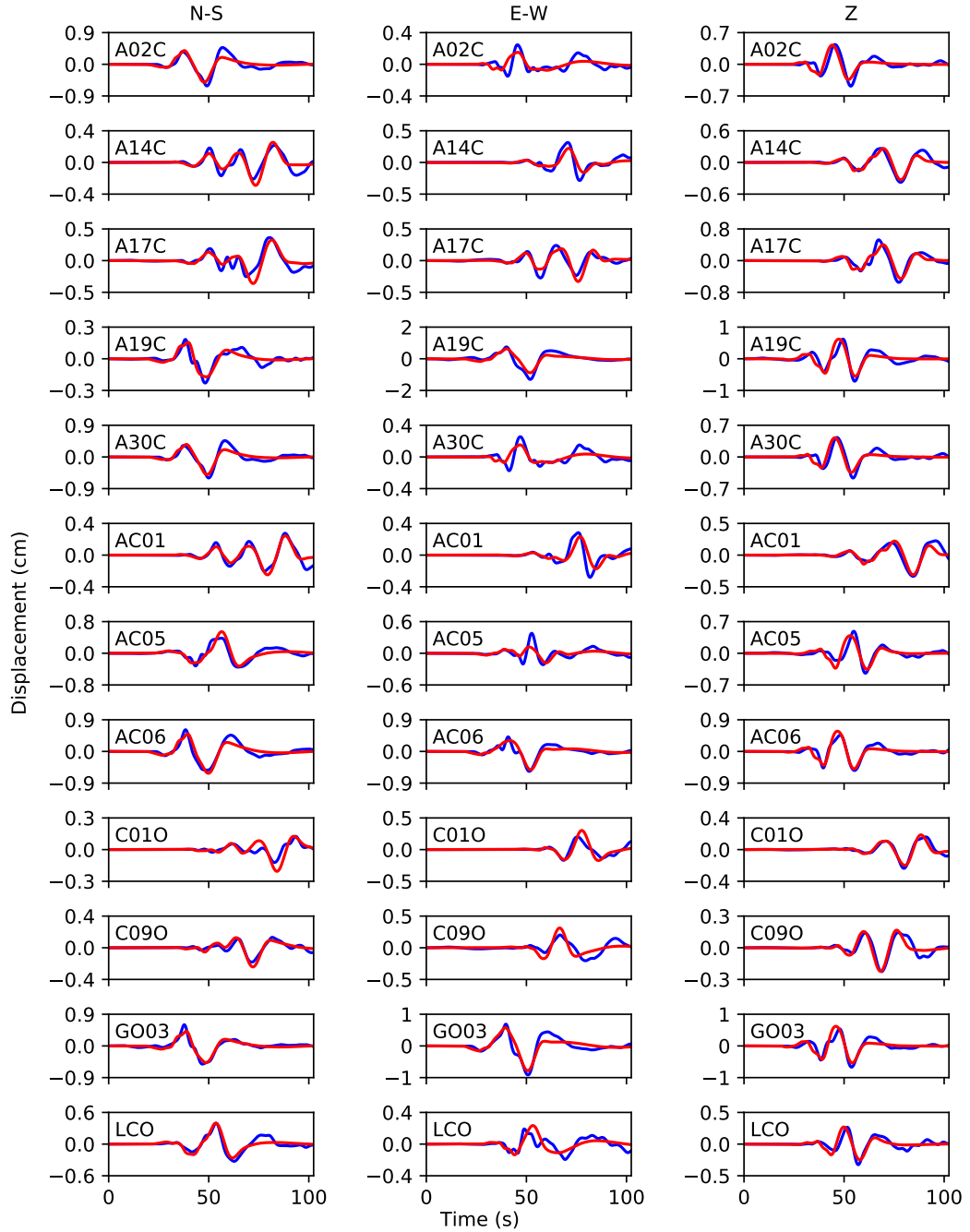


Figure S14. Main shock waveforms. Fit between the observed (blue) and modeled (red) seismograms of the best model obtained by the dynamic inversion. This corresponds to an overall L2 misfit of 0.24.

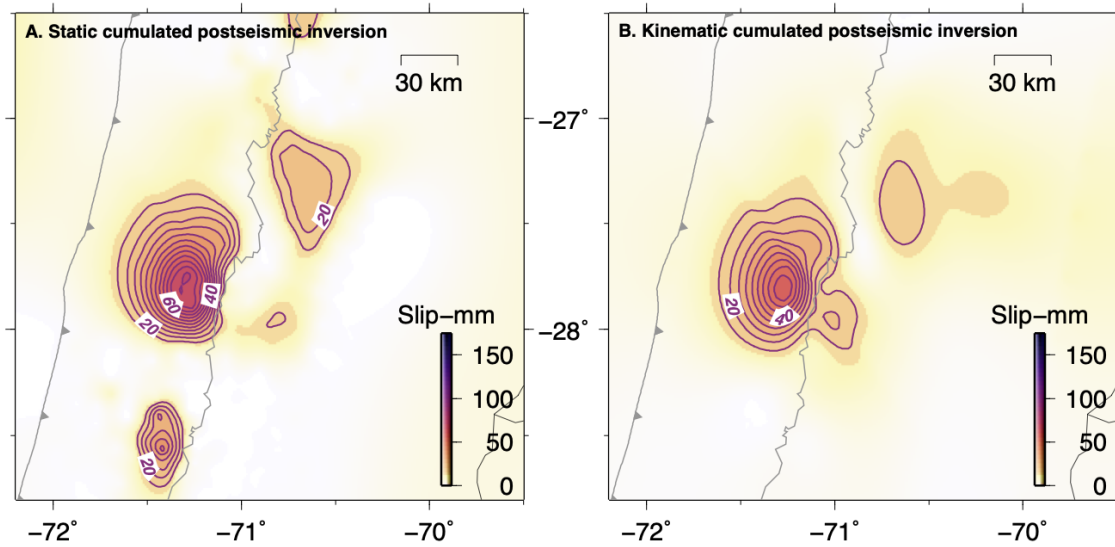


Figure S15. A: Slip distribution obtained by static inversion of the cumulative postseismic displacement field over 22 days; B: Slip distribution obtained by kinematic inversion of the cumulative postseismic displacements over the same period (shown on Fig. ??).

Mainshock 04:09

Sites	Lon	Lat	E	N	U	sE	sN	sU
BAR2	-70.788	-27.601	-14.49	-9.07	-1.90	1.9	2.9	7.1
BING	-70.858	-27.133	-2.42	-1.16	0.07	0.9	1.4	3.2
COP5	-70.016	-27.271	-3.19	-3.32	2.87	0.7	1.4	6.9
FMCO	-70.695	-26.577	-0.09	0.66	-1.97	0.9	1.0	3.2
HSCO	-71.227	-28.462	-2.01	-11.83	0.19	1.3	1.0	3.9
LLCH	-71.081	-28.190	-5.30	-11.40	12.20	1.4	3.8	3.6
MMOR	-70.640	-26.874	-1.53	-0.28	-1.36	0.9	0.8	4.0
MRCG	-69.130	-26.835	3.35	-1.84	0.40	1.4	2.1	4.1
PAZU	-70.599	-26.148	0.10	0.73	-2.01	0.8	1.0	3.0
TAMR	-70.236	-27.594	-9.28	-2.99	-1.19	1.0	1.5	4.2
TOT5	-70.340	-27.951	-13.32	0.01	-1.77	0.9	2.2	4.2
TRST	-70.270	-28.836	-4.21	0.38	-7.63	1.3	1.6	6.7
TTRL	-71.062	-27.884	-16.15	-1.86	9.31	2.3	6.6	6.0
UDAT	-70.354	-27.357	-7.24	-2.38	0.37	1.3	1.1	4.1

Aftershock 21:09

Sites	Lon	Lat	E	N	U	sE	sN	sU
BAR2	-70.788	-27.601	-3.62	-1.76	-4.48	1.9	2.9	7.1
BING	-70.858	-27.133	-0.06	-0.50	-2.07	0.9	1.4	3.2
COP5	-70.016	-27.271	-1.35	1.34	-6.86	0.7	1.4	6.9
FMCO	-70.695	-26.577	-0.64	-1.43	-0.95	0.9	1.0	3.2
HSCO	-71.227	-28.462	-0.11	-1.29	6.59	1.3	1.0	3.9
LLCH	-71.081	-28.190	-7.93	2.90	-3.94	1.4	3.8	3.6
MMOR	-70.640	-26.874	0.66	-0.69	1.55	0.9	0.8	4.0
MRCG	-69.130	-26.835	-3.42	1.76	3.91	1.4	2.1	4.1
PAZU	-70.599	-26.148	-0.02	-0.94	0.69	0.8	1.0	3.0
TAMR	-70.236	-27.594	-0.87	0.10	0.72	1.0	1.5	4.2
TOT5	-70.340	-27.951	-4.19	-0.15	-3.19	0.9	2.2	4.2
TRST	-70.270	-28.836	1.77	0.41	7.40	1.3	1.6	6.7
TTRL	-71.062	-27.884	-15.08	-4.30	-10.40	2.3	6.6	6.0
UDAT	-70.354	-27.357	0.42	-1.81	-2.05	1.3	1.1	4.1

Table S2. Tables of coseismic displacements estimated from daily CGPS for the 2 events (left table: main shock; right table: aftershock)

Mainshock 04:09

Sites	Lon	Lat	E	N	U	sE	sN	sU
BAR2	-70.788	-27.601	-10.1	-3.4	-12.3	2	2	5
BING	-70.858	-27.133	-3.0	-0.6	0.7	3	5	10
COP5	-70.016	-27.271	-1.4	0.0	4.0	5	5	10
FMCO	-70.695	-26.577	1.3	1.8	-9.5	3	3	10
HSCO	-71.227	-28.462	1.7	-7.1	-9.6	2	2	10
LLCH	-71.081	-28.190	-3.3	-9.4	4.6	2	2	5
MMOR	-70.640	-26.874	3.7	1.2	-5.8	3	3	5
TAMR	-70.236	-27.594	-8.5	-1.3	-7.1	3	5	10
TOT5	-70.340	-27.951	-14.1	1.6	-4.8	3	3	10
TRST	-70.270	-28.836	-3.0	2.1	-3.7	5	5	10
TTRL	-71.062	-27.884	-9.5	1.1	7.3	2	2	5
UDAT	-70.354	-27.357	-7.1	-0.2	-7.3	5	5	10

Aftershock 21:09

Sites	Lon	Lat	E	N	U	sE	sN	sU
BAR2	-70.788	-27.601	-4.0	-1.2	0.0	5	5	5
BING	-70.858	-27.133	0.0	0.0	0.0	5	5	10
COP5	-70.016	-27.271	0.0	0.0	0.0	5	5	10
FMCO	-70.695	-26.577	0.0	0.0	0.0	5	5	10
HSCO	-71.227	-28.462	0.0	0.0	0.0	5	5	10
LLCH	-71.081	-28.190	-5.2	4.5	0.0	5	5	5
MMOR	-70.640	-26.874	0.0	0.0	0.0	5	5	10
TAMR	-70.236	-27.594	0.0	0.0	0.0	5	5	10
TOT5	-70.340	-27.951	0.0	0.0	0.0	5	5	10
TRST	-70.270	-28.836	0.0	0.0	0.0	5	5	10
TTRL	-71.062	-27.884	-7.7	-2.5	0.0	5	5	5
UDAT	-70.354	-27.357	0.0	0.0	0.0	5	5	10

Table S3. Coseismic displacements estimated from HRGPS for the 2 events. All numbers in mm